COMPUTING EXPECTATION VALUES FOR MOLECULAR QUANTUM DYNAMICS

CAROLINE LASSER* AND SUSANNA RÖBLITZ†

Abstract. We compute expectation values for the solution of the nuclear Schrödinger equation. The proposed particle method consists of three steps: sampling of the initial Wigner function, classical transport of the sampling points, weighted phase space summation for the final computation of the expectation values. The Egorov theorem guarantees that the algorithm is second order accurate with respect to the semiclassical parameter. We present numerical experiments for a two-dimensional torsional potential with three different sets of initial data and for a six-dimensional Henon-Heiles potential. By construction, the computing times scale linearly with the number of initial sampling points and range between three seconds and one hour.

Key words. Time dependent Schrödinger equation, molecular quantum dynamics, expectation values, Wigner functions.

AMS subject classifications. 81S30, 81Q20, 81-08, 65D30, 65Z05

1. Introduction. The governing evolution equation of quantum molecular dynamics is the time dependent Schrödinger equation in semiclassical scaling,

$$\mathrm{i}\varepsilon\partial_t\psi^\varepsilon(t,q) = -\tfrac{\varepsilon^2}{2}\Delta_q\psi^\varepsilon(t,q) + V(q)\psi^\varepsilon(t,q), \qquad \psi^\varepsilon(0,q) = \psi_0^\varepsilon(q). \tag{1.1}$$

It describes the vibrational motion of a molecule's nuclei, if the key assumption of the time dependent Born-Oppenheimer approximation is satisfied [16]: The nuclei move in regions where for each nuclear configuration $q \in \mathbb{R}^d$ the governing electronic eigenvalue $V(q)$ is well separated from the rest of the electronic spectrum. It is a fundamental equation of femtosecond chemistry.

The initial wave function $\psi_0^\varepsilon : \mathbb{R}^d \to \mathbb{C}$ is square integrable with norm one,

$$\|\psi_0^\varepsilon\|_{L^2}^2 = \int_{\mathbb{R}^d} |\psi_0^\varepsilon(q)|^2 \mathrm{d}q = 1.$$

In many applications, it is a wave packet with a width of order $\sqrt{\varepsilon}$ and oscillations of wave length ε, as for example a Gaussian wave packet in semiclassical scaling,

$$\psi_0^\varepsilon(q) = (\pi\varepsilon)^{-d/4} \exp(-\tfrac{1}{2\varepsilon}|q-q_0|^2 + \tfrac{\mathrm{i}}{\varepsilon}\, p_0 \cdot (q-q_0)). \tag{1.2}$$

The small semiclassical parameter $\varepsilon > 0$ reflects the square root of the quotient of the electronic and average nuclear mass. Typically, it ranges between 0.001 and 0.1.

Away from electronic eigenvalue crossings, the potential energy surface $q \mapsto V(q)$ is smooth and bounded from below [8]. Therefore the solution

$$\psi^\varepsilon(t,q) = \mathrm{e}^{-\mathrm{i}\,(-\frac{\varepsilon^2}{2}\Delta_q + V(q))t/\varepsilon}\psi_0^\varepsilon(q)$$

of the Schrödinger equation (1.1) stems from a one-parameter group of unitary operators and is uniquely defined for all times t. The dimension d of the configuration space $\mathbb{R}^d$ is three times the number of nuclei in the molecule. Hence, nuclear quantum

†Zuse Institute Berlin (ZIB), Takustraße 7, 14195 Berlin, Germany, susanna.roeblitz@zib.de

*Freie Universität Berlin, Fachbereich Mathematik und Informatik, Arnimallee 6, 14195 Berlin, Germany, lasser@math.fu-berlin.de

motion poses a linear partial differential equation on a high dimensional configuration space. Moreover, the solution approximately inherits the localization and oscillation properties of the initial data and is therefore a highly oscillatory function with small functional support.

Our investigation has been motivated by recent work of E. Faou, V. Gradinaru, and C. Lubich on computing the time evolution $t \mapsto \psi^\varepsilon(t)$ using Hagedorn wave packets [4, 11]. Our approach is complementary and based on the current opinion that the wave function itself does not have any direct physical interpretation. The connection to experiment comes from expectation values

$$\langle \mathrm{op}_\varepsilon(a)\psi, \psi\rangle_{L^2} = \int_{\mathbb{R}^d} (\mathrm{op}_\varepsilon(a)\psi)(q)\,\overline{\psi}(q)\mathrm{d}q,$$

where $\mathrm{op}_\varepsilon(a)$ is a linear operator acting on subspaces of square integrable functions. Typical examples are the operator of the kinetic energy, the potential energy, or the total energy:

$$\psi \mapsto -\tfrac{\varepsilon^2}{2}\Delta_q\psi, \qquad \psi \mapsto V\psi, \qquad \psi \mapsto \tfrac{\varepsilon^2}{2}\Delta_q\psi + V\psi.$$

It is our aim here to directly compute expectation values using the Egorov theorem. The operators $\mathrm{op}_\varepsilon(a)$ are obtained as the Weyl quantization of smooth functions $a : \mathbb{R}^{2d} \to \mathbb{C}$, $(q,p) \mapsto a(q,p)$ on classical phase space, the space of positions and momenta. The action of $\mathrm{op}_\varepsilon(a)$ on a wave function is defined as

$$(\mathrm{op}_\varepsilon(a)\psi)(q) = (2\pi\varepsilon)^{-d} \int_{\mathbb{R}^{2d}} a(\tfrac{1}{2}(q+y),p)\mathrm{e}^{\mathrm{i}p\cdot(q-y)/\varepsilon}\psi(y)\mathrm{d}y\mathrm{d}p,$$

where the integral expression has to be read in the proper sense if the functions a and ψ are not integrable. Simple computations using the Fourier inversion formula yield that the operators of kinetic, potential, and total energy are obtained from the functions

$$a(q,p) = \tfrac{1}{2}|p|^2, \qquad a(q,p) = V(q), \qquad a(q,p) = \tfrac{1}{2}|p|^2 + V(q).$$

Let $\Phi^t : \mathbb{R}^{2d} \to \mathbb{R}^{2d}$ denote the flow of the Hamiltonian system

$$\dot{q} = p, \qquad \dot{p} = -\nabla V(q). \tag{1.3}$$

For the solution of the Schrödinger equation (1.1) and general Weyl quantized operators $\mathrm{op}_\varepsilon(a)$, the Egorov theorem gives

$$\langle \mathrm{op}_\varepsilon(a)\psi^\varepsilon(t), \psi^\varepsilon(t)\rangle_{L^2} = \big\langle \mathrm{op}_\varepsilon(a\circ\Phi^t)\psi_0^\varepsilon, \psi_0^\varepsilon\big\rangle_{L^2} + O(\varepsilon^2), \tag{1.4}$$

see for example [1, Theorem 1.2]. That is, for an asymptotic approximation with second order accuracy in ε no oscillations in time have to be resolved, and only the expectation value for the initial data has to be computed with respect to an operator, whose symbol is classically evolved in time. A closer examination reveals the well-known fact that the error term is dominated by third order derivatives of the potential and grows linearly in time. Thus for harmonic potentials, the Egorov description is exact. Moreover, the total energy is a conserved quantity for the Egorov approximation as it is for the solution of the Schrödinger equation, see §2 later on.

The approximation (1.4) turns into a particle method by the following observation. Expectation values for Weyl quantized operators can be expressed as phase space integrals of the wave function's Wigner function,

$$\langle \mathrm{op}_\varepsilon(a)\psi,\psi\rangle_{L^2} = \int_{\mathbb{R}^{2d}} a(q,p)W(\psi)(q,p)\mathrm{d}q\mathrm{d}p.$$

The Wigner function $W(\psi):\mathbb{R}^{2d}\to\mathbb{R}$ is the inverse Fourier transform of the autocorrelation function,

$$W(\psi)(q,p) = (2\pi\varepsilon)^{-d}\int_{\mathbb{R}^d} \mathrm{e}^{\mathrm{i}p\cdot y/\varepsilon}\psi(q-\tfrac{1}{2}y)\overline{\psi}(q+\tfrac{1}{2}y)\mathrm{d}y.$$

It is a continuous real-valued function on phase space. If $\|\psi\|_{L^2}=1$, then

$$\int_{\mathbb{R}^{2d}} W(\psi)(q,p)\,\mathrm{d}q\mathrm{d}p = 1.$$

The Gaussian wave packet (1.2) has a phase space Gaussian as its Wigner function,

$$W(\psi_0^\varepsilon)(q,p) = (\pi\varepsilon)^{-d}\exp(-\tfrac{1}{\varepsilon}|(q,p)-(q_0,p_0)|^2).$$

In terms of the Wigner function, the Egorov approximation (1.4) can be rephrased as

$$\langle \mathrm{op}_\varepsilon(a)\psi^\varepsilon(t),\psi^\varepsilon(t)\rangle_{L^2} = \int_{\mathbb{R}^{2d}} (a\circ\Phi^t)(q,p)\,W(\psi_0^\varepsilon)(q,p)\,\mathrm{d}q\mathrm{d}p + O(\varepsilon^2),$$

such that the numerical computation of expectation values is reduced to a three-step procedure involving phase space sampling of the initial Wigner function, classical transport of the sampling points according to (1.3) and final phase space summation over the propagated sampling points. In contrast to [12] this algorithmic interpretation of the Egorov theorem does not aim at computing observables in the limit $\varepsilon\to 0$ but for a fixed value of the semiclassical parameter $\varepsilon>0$.

The article is organized as follows. In §2 we review the proof of the Egorov theorem carefully discussing the error term and the propagation of sampling inaccuracies. §3 contains a short exposition of Monte Carlo and quasi-Monte Carlo sampling strategies for the initial Wigner function. Then, §4 bundles some preparatory numerical considerations on computing times and the discretization of the governing Hamiltonian systems. In §5 numerical experiments for a two-dimensional torsional potential and different types of initial data are presented. §6 concludes with the simulation for a six-dimensional Henon-Heiles potential.

2. The Egorov theorem. We reexamine the established proof of the Egorov theorem [1, Theorem 1.2] for analysing the error term. The Schrödinger operator is written as

$$\mathrm{op}_\varepsilon(h) = -\tfrac{\varepsilon^2}{2}\Delta_q + V(q)$$

with the symbol $h(q,p)=\frac{1}{2}|p|^2+V(q)$, and the solution of the Schrödinger equation (1.1) is expressed in terms of the unitary propagator

$$\psi^\varepsilon(t) = \mathrm{e}^{-\mathrm{i}\,\mathrm{op}_\varepsilon(h)t/\varepsilon}\psi_0^\varepsilon.$$

In what follows, we estimate the difference between the expectation values

$$\langle \mathrm{op}_\varepsilon(a)\psi^\varepsilon(t),\psi^\varepsilon(t)\rangle_{L^2} - \big\langle \mathrm{op}_\varepsilon(a\circ\Phi^t)\psi_0^\varepsilon,\psi_0^\varepsilon\big\rangle_{L^2}$$

by analyzing the difference

$$\mathrm{e}^{\mathrm{i}\,\mathrm{op}_\varepsilon(h)t/\varepsilon}\mathrm{op}_\varepsilon(a)\mathrm{e}^{-\mathrm{i}\,\mathrm{op}_\varepsilon(h)t/\varepsilon} - \mathrm{op}_\varepsilon(a\circ\Phi^t).$$

We give a formal outline of the argumentation.

$$\begin{aligned}
&\mathrm{e}^{\mathrm{i}\,\mathrm{op}_\varepsilon(h)t/\varepsilon}\mathrm{op}_\varepsilon(a)\mathrm{e}^{-\mathrm{i}\,\mathrm{op}_\varepsilon(h)t/\varepsilon} - \mathrm{op}_\varepsilon(a\circ\Phi^t) = \\
&\int_0^t \tfrac{\mathrm{d}}{\mathrm{d}s}\left(\mathrm{e}^{\mathrm{i}\,\mathrm{op}_\varepsilon(h)s/\varepsilon}\mathrm{op}_\varepsilon(a\circ\Phi^{t-s})\mathrm{e}^{-\mathrm{i}\,\mathrm{op}_\varepsilon(h)s/\varepsilon}\right)\mathrm{d}s = \\
&\int_0^t \mathrm{e}^{\mathrm{i}\,\mathrm{op}_\varepsilon(h)s/\varepsilon}\left(\tfrac{\mathrm{i}}{\varepsilon}\left[\mathrm{op}_\varepsilon(h),\mathrm{op}_\varepsilon(a\circ\Phi^{t-s})\right] - \mathrm{op}_\varepsilon(\partial_t(a\circ\Phi^{t-s}))\right)\mathrm{e}^{-\mathrm{i}\,\mathrm{op}_\varepsilon(h)s/\varepsilon}\mathrm{d}s.
\end{aligned}$$

For the time derivative one computes

$$\partial_t(a\circ\Phi^{t-s}) = (\partial_p h\cdot\partial_q a - \partial_q h\cdot\partial_p a)\circ\Phi^{t-s} = \{h,a\}\circ\Phi^{t-s} = \{h,a\circ\Phi^{t-s}\},$$

using that the classical flow as a symplectic transformation of phase space preserves the Poisson bracket. The commutator of Weyl quantized operators is again a Weyl quantized operator with a well-known asymptotic expansion in odd powers of the semiclassical parameter,

$$\tfrac{\mathrm{i}}{\varepsilon}\left[\mathrm{op}_\varepsilon(h),\mathrm{op}_\varepsilon(a\circ\Phi^{t-s})\right] = \tfrac{\mathrm{i}}{\varepsilon}\,\mathrm{op}_\varepsilon(b_\varepsilon)$$

with $b_\varepsilon \sim \sum_{j=0}^\infty \varepsilon^{2j+1}\, b_{2j+1}$ and

$$b_j(q,p) = 2\cdot(2\mathrm{i})^{-j}\sum_{|\alpha|+|\beta|=j}\frac{(-1)^{|\alpha|}}{\alpha!\beta!}\,\partial_q^\alpha\partial_p^\beta h(q,p)\,\partial_q^\beta\partial_p^\alpha(a\circ\Phi^{t-s})(q,p), \qquad j\geq 0.$$

Since the Hamilton function $h(q,p) = \frac{1}{2}|p|^2 + V(q)$ does neither have mixed derivatives nor momentum derivatives of order greater than two, the expressions simplify to $b_1 = -\mathrm{i}\{h,a\circ\Phi^{t-s}\}$ and

$$b_j(q,p) = 2\cdot(2\mathrm{i})^{-j}\sum_{|\alpha|=j}\frac{(-1)^{|\alpha|}}{\alpha!}\,\partial_q^\alpha V(q)\,\partial_p^\alpha(a\circ\Phi^{t-s})(q,p), \qquad j\geq 3.$$

Therefore, there exists a smooth function $e_\varepsilon : \mathbb{R}^{2d}\to\mathbb{C}$ with $e_\varepsilon \sim \sum_{j=1}^\infty \varepsilon^{2j}\, b_{2j+1}$ such that

$$\mathrm{e}^{\mathrm{i}\,\mathrm{op}_\varepsilon(h)t/\varepsilon}\mathrm{op}_\varepsilon(a)\mathrm{e}^{-\mathrm{i}\,\mathrm{op}_\varepsilon(h)t/\varepsilon} - \mathrm{op}_\varepsilon(a\circ\Phi^t) = \int_0^t \mathrm{e}^{\mathrm{i}\,\mathrm{op}_\varepsilon(h)s/\varepsilon}\mathrm{op}_\varepsilon(\mathrm{i}\,e_\varepsilon)\mathrm{e}^{-\mathrm{i}\,\mathrm{op}_\varepsilon(h)s/\varepsilon}\mathrm{d}s.$$

At this point, we distinguish the following cases.

2.1. Harmonic potentials. If the potential function is a polynomial of degree less than or equal two, then $\partial_q^\alpha V(q) = 0$ for $|\alpha|\geq 3$ and $e_\varepsilon(q,p) = 0$, which implies

$$\langle\mathrm{op}_\varepsilon(a)\psi^\varepsilon(t),\psi^\varepsilon(t)\rangle_{L^2} = \left\langle\mathrm{op}_\varepsilon(a\circ\Phi^t)\psi_0^\varepsilon,\psi_0^\varepsilon\right\rangle_{L^2}.$$

Hence for harmonic motion all expectation values are exactly described by classical transport.

2.2. General potentials. The symbol $e_\varepsilon(q,p)$ contains terms of the form

$$\partial_q^\alpha V(q)\,\partial_p^\alpha (a\circ\Phi^{t-s})(q,p)$$

with $|\alpha|\geq 3$. Hence for bounding the norm of $\mathrm{op}_\varepsilon(e_\varepsilon)$ as an operator on $L^2(\mathbb{R}^d)$ one needs a smooth potential $V(q)$, whose derivatives of order larger or equal than three are bounded, and a smooth observable $a(q,p)$, whose derivatives are bounded. Indeed, by the Calderón-Vaillancourt theorem, see for example [5, Chapter 2.5] or [3, Theorem 7.11], there is a constant $C_{\mathrm{cv}}>0$ such that for all $\varepsilon>0$

$$\|\mathrm{op}_\varepsilon(e_\varepsilon)\|\leq C_{\mathrm{cv}}\sum_{|\alpha|\leq 2d+1}\varepsilon^{|\alpha|/2}\,\|\partial^\alpha e_\varepsilon\|_\infty.$$

Consequently, for each $t\in\mathbb{R}$ there exists $C_\varepsilon(t)>0$ such that for square integrable initial data with norm one

$$\left|\langle \mathrm{op}_\varepsilon(a)\psi^\varepsilon(t),\psi^\varepsilon(t)\rangle_{L^2}-\left\langle \mathrm{op}_\varepsilon(a\circ\Phi^t)\psi_0^\varepsilon,\psi_0^\varepsilon\right\rangle_{L^2}\right|\leq C_\varepsilon(t)\varepsilon^2 t.$$

The constant allows an asymptotic expansion

$$C_\varepsilon(t)\sim\sum_{j=0}^{\infty}\varepsilon^{j/2}c_j(t)$$

in powers of $\varepsilon^{1/2}$, where each coefficient $c_j(t)$ depends on derivatives of the potential $V(q)$ of the order $j+3$ and higher order derivatives of the observable $a(q,p)$ and the flow $\Phi^t(q,p)$.

2.3. Energy conservation. Since $\mathrm{op}_\varepsilon(h)$ and its unitary propagator $\mathrm{e}^{-\mathrm{i}\mathrm{op}_\varepsilon(h)t/\varepsilon}$ commute, the expectation value of the total energy

$$\langle \mathrm{op}_\varepsilon(h)\psi^\varepsilon(t),\psi^\varepsilon(t)\rangle_{L^2}=\langle \mathrm{op}_\varepsilon(h)\psi_0^\varepsilon,\psi_0^\varepsilon\rangle_{L^2}$$

is conserved for all times. By conservation of classical energy $h=h\circ\Phi^t$ we therefore also obtain

$$\langle \mathrm{op}_\varepsilon(h)\psi^\varepsilon(t),\psi^\varepsilon(t)\rangle_{L^2}=\left\langle \mathrm{op}_\varepsilon(h\circ\Phi^t)\psi_0^\varepsilon,\psi_0^\varepsilon\right\rangle_{L^2}.$$

Hence the total energy expectation value has an exact Egorov description.

2.4. Error propagation. The previous analysis does not account for possible inaccuracies of the initial sampling. In a numerical simulation, the expectation value $\langle \mathrm{op}(\tilde a)\psi_0^\varepsilon,\psi_0^\varepsilon\rangle_{L^2}$ of a slightly distorted observable $\tilde a(q,p)$ enters the propagation. Then we are interested in the time evolution of the difference

$$\mathrm{e}^{\mathrm{i}\,\mathrm{op}_\varepsilon(h)t/\varepsilon}\mathrm{op}_\varepsilon(a)\mathrm{e}^{-\mathrm{i}\,\mathrm{op}_\varepsilon(h)t/\varepsilon}-\mathrm{op}_\varepsilon(\tilde a\circ\Phi^t).$$

The linear combination $a_{t,s}=a+\frac{t-s}{t}(\tilde a-a)$ satisfies $a_{t,t}=a$ and $a_{t,0}=\tilde a$. Hence the previous line of argumentation yields

$$\begin{aligned}
&\mathrm{e}^{\mathrm{i}\,\mathrm{op}_\varepsilon(h)t/\varepsilon}\mathrm{op}_\varepsilon(a)\mathrm{e}^{-\mathrm{i}\,\mathrm{op}_\varepsilon(h)t/\varepsilon}-\mathrm{op}_\varepsilon(\tilde a\circ\Phi^t)=\\
&\int_0^t\tfrac{\mathrm{d}}{\mathrm{d}s}\left(\mathrm{e}^{\mathrm{i}\,\mathrm{op}_\varepsilon(h)s/\varepsilon}\mathrm{op}_\varepsilon(a_{t,s}\circ\Phi^{t-s})\mathrm{e}^{-\mathrm{i}\,\mathrm{op}_\varepsilon(h)s/\varepsilon}\right)\mathrm{d}s=\\
&\int_0^t\mathrm{e}^{\mathrm{i}\,\mathrm{op}_\varepsilon(h)s/\varepsilon}\left(\tfrac{\mathrm{i}}{\varepsilon}\left[\mathrm{op}_\varepsilon(h),\mathrm{op}_\varepsilon(a_{t,s}\circ\Phi^{t-s})\right]+\mathrm{op}_\varepsilon(\partial_s(a_{t,s}\circ\Phi^{t-s}))\right)\mathrm{e}^{-\mathrm{i}\,\mathrm{op}_\varepsilon(h)s/\varepsilon}\mathrm{d}s.
\end{aligned}$$

The first summand of the derivative

$$\partial_s(a_{t,s}\circ\Phi^{t-s}) = -\{h, a_{t,s}\circ\Phi^{t-s}\} - \tfrac{1}{t}(\tilde{a}-a)\circ\Phi^{t-s}$$

together with the commutator $\frac{\mathrm{i}}{\varepsilon}[\mathrm{op}_\varepsilon(h), \mathrm{op}_\varepsilon(a_{t,s}\circ\Phi^{t-s})]$ allows for the same analysis as before. The second summand suggests to measure the mean deviation of $\tilde{a}$ from a along the classical flow in terms of the time average

$$\delta_t(q,p) = \frac{1}{t}\int_0^t (\tilde{a}-a)\circ\Phi^s(q,p)\mathrm{d}s.$$

Then we obtain

$$\left|\langle \mathrm{op}_\varepsilon(a)\psi^\varepsilon(t), \psi^\varepsilon(t)\rangle_{L^2} - \left\langle \mathrm{op}_\varepsilon(\tilde{a}\circ\Phi^t)\psi_0^\varepsilon, \psi_0^\varepsilon\right\rangle_{L^2}\right| \le C_\varepsilon\varepsilon^2 + \|\mathrm{op}_\varepsilon(\delta_t)\|.$$

Since $\mathrm{op}_\varepsilon(\delta_t)$ can be bounded independently of ε using bounds on the derivatives of the difference $\tilde{a}-a$ along the flow, a small initial sampling error does not alter the asymptotic accuracy of the method.

3. Initial phase space sampling. For the first step of the algorithm the Wigner function of the initial data has to be sampled. In the literature, predominantly Gaussian wave packets with diagonal width matrix are considered. That is,

$$g_0^\varepsilon(q) = (\pi\varepsilon)^{-d/4}\det(D)^{1/4}\exp(-\tfrac{1}{2\varepsilon}(q-q_0)\cdot D(q-q_0) + \tfrac{\mathrm{i}}{\varepsilon}p_0\cdot(q-q_0)) \tag{3.1}$$

with $(q_0,p_0)\in\mathbb{R}^{2d}$ and $D=\mathrm{diag}(d_1,\dots,d_d)\in\mathbb{R}^{d\times d}$ positive definite. In this simple case, the Wigner function can be analytically calculated as a phase space Gaussian. Denoting $z=(q,p)$, $z_0=(q_0,p_0)$ and $D_2=\mathrm{diag}(d_1,\dots,d_d,d_1^{-1},\dots,d_d^{-1})$, it reads as

$$W(g_0^\varepsilon)(z) = (\pi\varepsilon)^{-d}\exp(-\tfrac{1}{\varepsilon}(z-z_0)\cdot D_2(z-z_0)). \tag{3.2}$$

We also consider the superposition of two Gaussian wave packets $n_{12}^\varepsilon(g_1^\varepsilon+g_2^\varepsilon)$ centered in $z_1,z_2\in\mathbb{R}^{2d}$ with the same diagonal width matrix D and a normalizing constant $n_{12}^\varepsilon>0$. An elementary calculation involving one-dimensional Gaussian integrals [10, Appendix B] yields

$$W(g_1^\varepsilon+g_2^\varepsilon)(z) = W(g_1^\varepsilon)(z) + W(g_2^\varepsilon)(z) + 2\,C(z)$$

with an oscillatory cross term

$$\begin{aligned} C(z) &= (\pi\varepsilon)^{-d}\exp(-\tfrac{1}{\varepsilon}(z-z_+)\cdot D_2(z-z_+))\cdot\cos(\tfrac{1}{\varepsilon}p_+\cdot q_- - \tfrac{1}{\varepsilon}(z-z_+)\wedge z_-) \\ &=: (\pi\varepsilon)^{-d}\exp(-\tfrac{1}{\varepsilon}(z-z_+)\cdot D_2(z-z_+))\cdot c(z), \end{aligned}$$

where $x\wedge y = p(x)\cdot q(y) - q(x)\cdot p(y)$ is the wedge product for vectors $x,y\in\mathbb{R}^{2d}$. The cross term localizes around the average $z_+=\frac{1}{2}(z_1+z_2)$ and oscillates with a frequency proportional to the distance $z_-=z_1-z_2$. The normalizing constant enters the Wigner function quadratically,

$$W(n_{12}^\varepsilon(g_1^\varepsilon+g_2^\varepsilon)) = (n_{12}^\varepsilon)^2\,W(g_1^\varepsilon+g_2^\varepsilon). \tag{3.3}$$

In general, one expects initial data which are wave packets with a width of order $\sqrt{\varepsilon}$ and oscillations of wave length of order ε or superpositions of such functions. Due to the high dimensionality of the problem we have explored quadrature approaches approximating the relevant phase space integral as

$$\langle a\circ\Phi^t\rangle_{\psi_0^\varepsilon} := \int_{\mathbb{R}^{2d}}(a\circ\Phi^t)(z)W(\psi_0^\varepsilon)(z)\,\mathrm{d}z \;\approx\; \frac{1}{N}\sum_{j=1}^N (a\circ\Phi^t)(x_j)$$

with uniform quadrature weight N^{-1} and two different choices for the quadrature nodes $\{x_j\}_{j=1}^N \subset \mathbb{R}^{2d}$. The methods discussed in the following are conventional Monte Carlo and quasi-Monte Carlo integration.

3.1. Conventional Monte Carlo. If the initial data is a single Gaussian wave packet $\psi_0^\varepsilon = g_0^\varepsilon$, then the Wigner function $W(g_0^\varepsilon)$ is a single Gaussian function in phase space, see (3.2). One reads this Wigner function as the density function of a multivariate normal distribution $\mathcal{N}$ with mean z_0 and covariance matrix $\frac{\varepsilon}{2} D_2^{-1}$ and draws N independent samples $x_1, \dots, x_N$ from it. By the central limit theorem, we have for all $c > 0$

$$\lim_{N\to\infty} \mathbb{P}\Big(\Big| \tfrac{1}{N} \textstyle\sum_{j=1}^N (a \circ \Phi^t)(x_j) - \langle a \circ \Phi^t \rangle_{\psi_0^\varepsilon} \Big| \le \tfrac{c\, \sigma(a\circ\Phi^t)}{\sqrt{N}} \Big) = \tfrac{1}{\sqrt{2\pi}} \int_{-c}^{c} \mathrm{e}^{-t^2/2} \mathrm{d}t,$$

where $\sigma(a \circ \Phi^t)$ is the standard deviation of $a \circ \Phi^t$,

$$\sigma(a \circ \Phi^t)^2 = \int_{\mathbb{R}^{2d}} \big((a \circ \Phi^t)(z) - \langle a \circ \Phi^t \rangle_{\psi_0^\varepsilon} \big)^2 \, W(g_0^\varepsilon)(z) \, \mathrm{d}z.$$

For the superposition of two Gaussian wave packets $\psi_0^\varepsilon = n_{12}^\varepsilon (g_1^\varepsilon + g_2^\varepsilon)$ we use a stratified sampling strategy. In this case, the initial Wigner function (3.3) is a sum of two phase space Gaussians centered around z_1 and z_2 plus an oscillatory cross term with Gaussian envelope function centered around z_+. Consequently one generates three sets of normally distributed sampling points with mean z_1, z_2, and z_+, respectively. The approximation for the expectation value $\langle a \circ \Phi^t \rangle_{\psi_0^\varepsilon}$ is

$$\frac{(n_{12}^\varepsilon)^2}{N} \sum_{j=1}^{N} \big((a \circ \Phi^t)(x_j(z_1)) + (a \circ \Phi^t)(x_j(z_2)) + (a \circ \Phi^t)(x_j(z_+)) \cdot 2c(x_j(z_+)) \big). \tag{3.4}$$

To avoid cancellation in the summation of the oscillatory cross term, positive and negative contributions are summed separately, see [2, Chapter 2.2]. The plot in Figure 4.1(a) illustrates the expected convergence rate of the order $N^{-1/2}$ for a two-dimensional test case. The semiclassical parameter is $\varepsilon = 0.1$ and the two Gaussian wave packets with width matrix $D = \mathrm{Id}$ are centered in $z_1 = (1, 0, 0, 0)$ and $z_2 = -z_1$.

3.2. Quasi-Monte Carlo. We return to the single Gaussian wave packet g_0^ε and explore a more accurate, deterministic alternative for the integration using quadrature points of low discrepancy. Again one views $W(g_0^\varepsilon)$ as the density function of the multivariate normal distribution $\mathcal{N}$ but generates deterministic points $\{x_j\}_{j=1}^N$ with low star-discrepancy

$$D_{\mathcal{N}}^*(x_1, \dots, x_N) = \sup_{a \in \mathbb{R}^{2d}} \big| N^{-1} \cdot \sharp\{x_j \mid x_j \in (-\infty, a),\, j = 1, \dots N\} - \mathcal{N}((-\infty, a)) \big|$$

where $(-\infty, a) = \prod_{n=1}^{2d} (-\infty, a_n)$ is the open $2d$-dimensional interval with upper bound $a \in \mathbb{R}^{2d}$. The Gaussian Wigner function (3.2) separates as

$$W(g_0^\varepsilon)(z) = \prod_{n=1}^{2d} \sqrt{\frac{\alpha_n}{\varepsilon\pi}} \, \exp\big(-\tfrac{\alpha_n}{\varepsilon} (z_n - z_{0,n})^2 \big),$$

where $\alpha = (d_1, \dots, d_d, d_1^{-1}, \dots, d_d^{-1})$ is the vector defining the diagonal matrix D_2. Therefore the inverse distribution function of $\mathcal{N}$ is given explicitly as

$$F_{\mathcal{N}}^{-1} : (0,1)^{2d} \to \mathbb{R}^{2d}, \quad F_{\mathcal{N}}^{-1}(w)_n = \sqrt{\tfrac{\varepsilon}{\alpha_n}} \, \mathrm{erf}^{-1}(2w_n - 1) + z_{0,n}.$$

On the unit cube $[0,1)^{2d}$ there exist several well-known sequences $(y_j)_{j\geq 1}$ of low star-discrepancy with respect to the uniform distribution $\mathcal{U}$ as for example the Halton or the Sobol' sequences. They obey

$$\begin{aligned} D^*_{\mathcal{U}}(y_1,\dots,y_N) &= \sup_{a\in[0,1)^{2d}} \left| N^{-1}\cdot \sharp\{y_j \mid y_j\in[0,a),\, j=1,\dots N\} - \mathcal{U}([0,a))\right| \\ &\leq C_{2d}\, N^{-1}(\log N)^{2d}, \end{aligned}$$

where the constant $C_{2d}>0$ is different for each sequence, see for example [14, Section 1.1]. The points $x_j = F^{-1}_{\mathcal{N}}(y_j)$, $j=1,\dots,N$, generated by the inversion method inherit this favorable property and also satisfy

$$D^*_{\mathcal{N}}(x_1,\dots,x_N) \leq C_{2d}\, N^{-1}(\log N)^{2d}. \tag{3.5}$$

Let $\mathcal{F}$ denote the space of smooth functions $f:\mathbb{R}^{2d}\to\mathbb{R}$ which eventually become constant. That is, for each $f\in\mathcal{F}$ there exists $R>0$ such that $f(z)=f(\pi_R(z))$ for all $z\notin Q_R$, where $Q_R=\{z\in\mathbb{R}^{2d} : |z_j|\leq R,\, j=1,\dots 2d\}$ is the closed cube of side length R and $\pi_R:\mathbb{R}^{2d}\to Q_R$ the orthogonal projection onto the cube. These functions have a limit as z tends to infinity, that is, $\lim_{\|z\|\to\infty} f(z) = f(R,\dots,R)$. Moreover, they are of bounded variation in the sense of Hardy and Krause [15, Chapter 2.2]. That is,

$$\mathrm{Var}(f) = \sum_{\emptyset\neq I\subseteq\{1,\dots,2d\}} \int_{Q_R} \frac{\partial^{|I|}}{\partial z_I} f(z_I,\mathbf{R}_{I^c})\,\mathrm{d}z < \infty,$$

where $\frac{\partial^{|I|}}{\partial z_I} f(z_I,\mathbf{R}_{I^c})$ means that at coordinates $j\notin I$ the mixed derivative $\frac{\partial^{|I|}}{\partial z_I} f$ is evaluated at $z_j=R$. Therefore established results on unbounded, weighted quasi-Monte Carlo integration apply, and the proof of [7, Theorem 3.4] yields a Koksma-Hlawka inequality of the form

$$\left| \frac{1}{N}\sum_{j=1}^{N} f(x_j) - \int_{\mathbb{R}^{2d}} f(z) W(g_0^\varepsilon)(z)\mathrm{d}z \right| \;\leq\; \mathrm{Var}(f)\, D^*_{\mathcal{N}}(x_1,\dots,x_N).$$

In our case, however, the integrands $a\circ\Phi^t$ do not belong to the space $\mathcal{F}$. Nevertheless, the numerical experiments show a convergence rate for the initial sampling, which is slightly worse than of the order N^{-1}. Figure 4.1(b) illustrates the error for the computation of several expectation values of the superposition of two Gaussian wave packets obtained by a stratified sampling approach analogously to (3.4).

This is due to the exponential decay of the Gaussian weight function, which yields

$$\int_{\mathbb{R}^{2d}\setminus Q_R} (a\circ\Phi^t)(z) W(g_0^\varepsilon)(z)\mathrm{d}z = O(N^{-1})$$

for cubes with side length $R=O((\log N)^{1/2})$, see also [13, Section 4.1]. Let $f_R(z) = (a\circ\Phi^t)(z)$ for $z\in Q_R$ and $f_R(z)=(a\circ\Phi^t)(\pi_R(z))$ for $z\notin Q_R$. Then

$$\mathrm{Var}(f_R) \leq \mathrm{vol}(Q_R) \sum_{\emptyset\neq I\subseteq\{1,\dots,2d\}} \|\tfrac{\partial^{|I|}}{\partial w_I} f_R\|_\infty = O((\log N)^d),$$

and the expected rate of convergence for the quasi-Monte Carlo integration slightly deteriorates to the order of $N^{-1}(\log N)^{2d+d}$, which is hardly observable in numerical experiments.

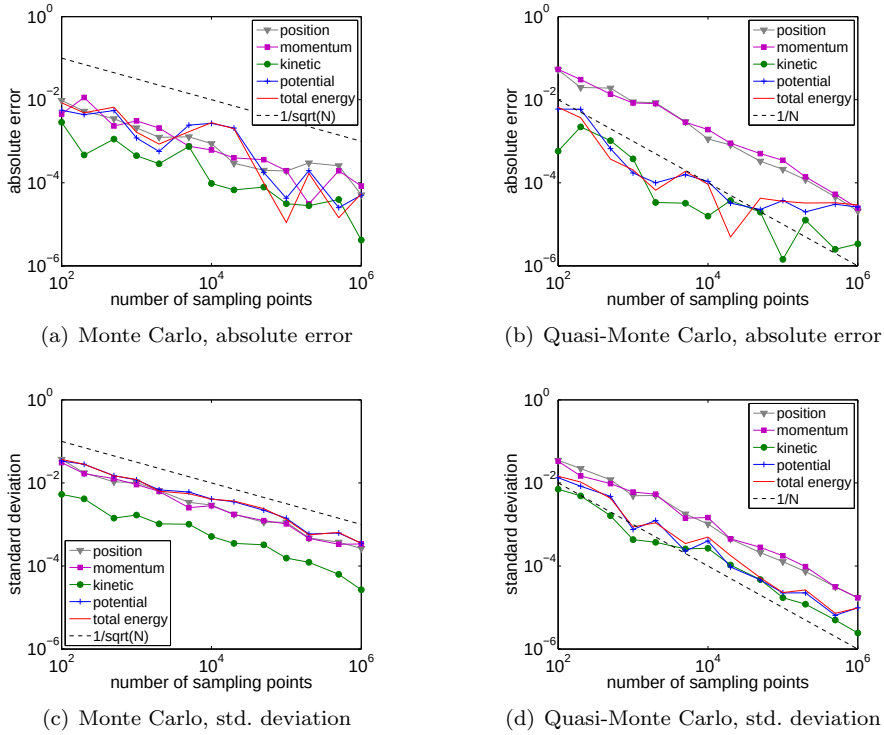

(a) Monte Carlo, absolute error

(b) Quasi-Monte Carlo, absolute error

(c) Monte Carlo, std. deviation

(d) Quasi-Monte Carlo, std. deviation

FIG. 4.1. *Initial sampling. We explore the accuracy of the computation of the initial expectation values with respect to the number N of sampling points. The wave function is the superposition of two-dimensional Gaussian wave packets (4.1). The error is the mean absolute error of ten independent runs of the sampling, where the quasi-Monte Carlo runs use randomly selected prime bases. As expected, the Monte Carlo convergence rate is of the order $N^{-1/2}$. The quasi-Monte Carlo error is slightly worse than of the order of N^{-1}. The associated standard deviations show a similar behavior.*

4. Preparatory numerical considerations. To begin with we discuss the efficiency of available numerical routines with respect to computing time and accuracy. Note that all experiments are performed with MATLAB 7.5 on a 2.2 GHz AMD Opteron Dual Core 875 Processor.

4.1. Initial sampling. We compare the initial Monte Carlo and quasi-Monte Carlo sampling for the two-dimensional superposition of Gaussian wave packets

$$\psi_0^\varepsilon = n_{12}^\varepsilon(g_1^\varepsilon + g_2^\varepsilon), \qquad z_1 = (1,0,0,0)^T, \qquad z_2 = -z_1, \qquad \varepsilon = 0.1 \tag{4.1}$$

with width matrix $D = \mathrm{Id}$ and normalizing constant $n_{12}^\varepsilon \approx 1/\sqrt{2}$ in terms of accuracy and computing time. The Wigner function $W(\psi_0^\varepsilon) = (n_{12}^\varepsilon)^2(W(g_1^\varepsilon) + W(g_2^\varepsilon) + 2C)$ is a sum of two phase space Gaussians plus an oscillatory cross term with Gaussian envelope. In this case the kinetic energy and the potential energy for the torsional potential

$$V(q) = 2 - \cos(q_1) - \cos(q_2) \tag{4.2}$$

can be computed analytically, since

$$\int_{\mathbb{R}^4} \tfrac{1}{2}|p|^2\, W(g_j^\varepsilon)(q,p)\,\mathrm{d}q\mathrm{d}p = \tfrac{1}{2}(\varepsilon + p_{j,1}^2 + p_{j,2}^2), \qquad j=1,2$$

$$\int_{\mathbb{R}^4} \tfrac{1}{2}|p|^2\, C(q,p)\,\mathrm{d}q\mathrm{d}p = \tfrac{1}{2}\,\mathrm{e}^{-1/\varepsilon}(\varepsilon - 1),$$

$$\int_{\mathbb{R}^4} V(q)\, W(g_j^\varepsilon)(q,p)\,\mathrm{d}q\mathrm{d}p = 2 - \mathrm{e}^{-\varepsilon/4}\left(\cos(q_{j,1}) + \cos(q_{j,2})\right), \qquad j=1,2$$

$$\int_{\mathbb{R}^4} V(q)\, C(q,p)\,\mathrm{d}q\mathrm{d}p = \mathrm{e}^{-1/\varepsilon}(2 - 2\mathrm{e}^{-\varepsilon/4}).$$

These formulas are used for evaluating the initial sampling error for all energy expectation values in the following numerical experiments.

The Monte Carlo points are generated by the MATLAB routine randn(). To obtain statistical evidence one has to work with the mean of several independent sampling runs. For the quasi-Monte Carlo integration we consider Halton sequences generated by the MATLAB routine vdcorput()[1]. Different runs use different prime bases selected randomly from the first 100 primes. Monte Carlo integration achieves a convergence rate of the order $N^{-1/2}$, while the quasi-Monte Carlo method yields an accuracy slightly worse than of the order N^{-1}. The absolute errors as well as the standard deviations in Figure 4.1 for the initial expectation values of position, momentum, kinetic, potential, and total energy confirm this expectation. Note that due to the stratified sampling approach, the total number N of sampling points is three times the number indicated along the x-axis in the two plots.

The convergence of the quasi-Monte Carlo error, see Figure 4.1(b), stagnates below 10^{-5}. This reflects the contribution of the cross term ($\exp(-1/\varepsilon) \simeq 4.54 \cdot 10^{-5}$ for $\varepsilon = 0.1$) and hints to the fact that it has not been sampled with sufficient accuracy. In fact, as long as the desired tolerance for the absolute error is larger than the contribution of the cross term, the simulation of $C(q,p)$ can be neglected (see also §5.2).

Both the generation of the normally distributed points and the Halton points can be done efficiently in a vectorized way. The approximate computing times scale linearly with the number of points and runs, see Table 4.1. However, the quasi-Monte Carlo approach takes considerably more time than the Monte Carlo method for the same number N of sampling points.

TABLE 4.1

Initial sampling. We explore approximate computing times and memory requirement for the initial sampling of the Wigner function with N points. The wave function is the superposition of two-dimensional Gaussian wave packets (4.1). The computing times scale about linearly with the number of points and runs.

	memory	Monte Carlo (1 run/10 runs)	quasi-Monte Carlo
$N = 3 \cdot 10^4$	0.92 MB	0.07 sec/0.26 sec	3.09 sec
$N = 3 \cdot 10^6$	92 MB	3.18 sec/32 sec	316 sec

4.2. Propagation. The analysis of §2.3 suggests that the particle method conserves the total energy expectation value over time. We explore this conservation

[1] http://www.mathworks.de/matlabcentral/fileexchange/15354

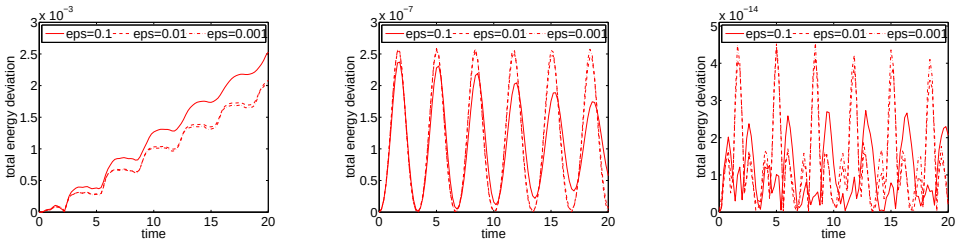

(a) ode45 (b) Störmer-Verlet (c) SPRK4

FIG. 4.2. *Energy conservation. We show the time-evolution of the absolute difference between the numerically computed initial total energies and the numerically computed values of the total energy for a single Gaussian wave packet sampled with $N = 10^4$ Halton points. The non-symplectic Runge-Kutta method* ode45 *causes a drift in the total energy, while the symplectic Störmer-Verlet and SPRK4 integrator are accurate to second and fourth order, respectively.*

property for an initial Gaussian wave packet centered in $z_1 = (1, 0, 0, 0)^T$ sampled with $N = 10^4$ Halton points. The Schrödinger equation with torsional potential (4.2) is considered for the semiclassical parameters $\varepsilon = 0.1$, 0.01, and 0.001 and fixed time interval $[0, 20]$. We compare the fourth order Runge-Kutta method with adaptive time stepping (MATLAB function ode45 with default parameters), the second order Störmer-Verlet scheme and the fourth order symplectic partitioned Runge-Kutta method SPRK4, see [6, Chapter VI.4]. For both symplectic schemes we use the time step $\tau = 0.1 \cdot 2^{-6} \simeq 0.0016$. The computing time with ode45 (100.8 sec) is about twice as large as for SPRK4 (54.6 sec) and four times larger than for Störmer-Verlet (22.7 sec). Since the ode45 integrator is not symplectic, it leads to a drift of energy, whereas the Störmer-Verlet and the SPRK4 method preserve the total energy within an accuracy of $\tau^2 \simeq 2 \cdot 10^{-6}$ and $\tau^4 \simeq 6 \cdot 10^{-12}$, respectively, see the plots in Figure 4.2.

We want the time integration to be more accurate than the statistical error of the sampling and the propagation error predicted by the Egorov theorem for the smallest value $\varepsilon = 0.001$ ($\varepsilon^2 = 10^{-6}$). For this reason, the integrator SPRK4 with time step $\tau = 0.1 \cdot 2^{-6}$ is used throughout all following numerical experiments, even though a larger time step of about $\tau = 0.01$ would have been sufficient.

5. The torsional potential. In this section, we consider the time dependent Schrödinger equation (1.1) in two dimensions with the torsional potential

$$V(q) = 2 - \cos(q_1) - \cos(q_2).$$

For the semiclassical parameter we choose the three different values $\varepsilon = 0.1$, 0.01, and 0.001. The time-interval is always $[0, 20]$. The initial data are of the following three types.

A. The single Gaussian wave packet

$$\psi_0^\varepsilon(q) = g_0^\varepsilon(q) = (\pi\varepsilon)^{-1/2} \exp(-\tfrac{1}{2\varepsilon}|q - q_0|^2), \qquad z_0 = (q_0, p_0) = (1, 0, 0, 0)^T.$$

B. The superposition of two Gaussian wave packets

$$\psi_0^\varepsilon = n_{12}^\varepsilon (g_1^\varepsilon + g_2^\varepsilon), \qquad z_1 = (1, 0, 0, 0)^T, \qquad z_2 = -z_1$$

where the normalizing constant is roughly $n_{12}^\varepsilon \approx 1/\sqrt{2}$.

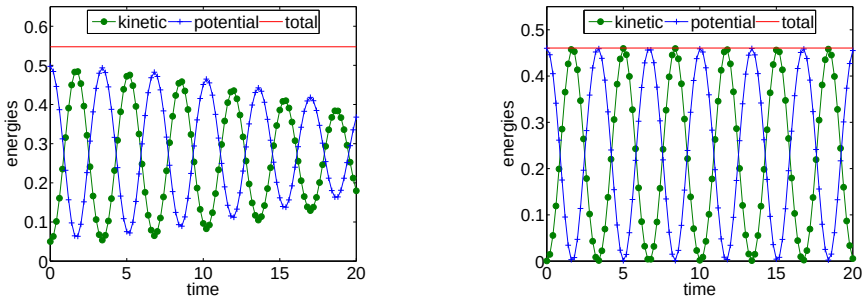

(a) $\varepsilon = 0.1$ (b) $\varepsilon = 0.001$

FIG. 5.1. *Evolution of kinetic, potential and total energy for the torsional potential and two different values of ε. The initial wave function is the Gaussian wave packet (A). The initial distribution is sampled with $N = 10^4$ Halton points. The computing time is 54.6 seconds.*

C. The function $\psi_0^\varepsilon = \phi_0^\varepsilon$, which stems from the numerical simulation of the laser excitation of a triatomic molecule. For the generation of this wave function a two-level Schrödinger system with time dependent electric field is solved for Gaussian initial data centered at $z_3 = (0.5, 0.05, -1, 0)$, see [10, Section 5.2] for details. The contour plot of the position density $q \mapsto |\phi_0^\varepsilon(q)|^2$ in Figure 5.6(a) shows a wave function of slightly distorted circular form.

TABLE 5.1

Approximate computing times for a single run of the algorithm for the two-dimensional torsional potential. The initial data are a Gaussian wave packet (A), a superposition of Gaussian wave packets (B) and a laser excited wave function (C). By construction, the computing times scale linearly in the number of sampling points N.

	A ($\varepsilon = 0.001$)	B ($\varepsilon = 0.1$)	C ($\varepsilon = 0.01$)
$N = 3 \cdot 10^3$	16.4 sec	15.9 sec	38.8 sec
$N = 3 \cdot 10^4$	2 min 45 sec	2 min 44 sec	6 min 39 sec
$N = 3 \cdot 10^5$	31 min 16 sec	31 min	64 min

Before discussing the numerical results in more detail, we summarize the approximate computing times. For the Gaussian wave packets and the superpositions thereof the computing time is dominated by the propagation of particles. Table 5.1 shows comparable run times for both types of initial data ranging from 16 seconds for $N = 3 \cdot 10^3$ sampling points to 31 minutes for $N = 3 \cdot 10^5$ points. For the laser excited initial data the situation is different, since the initial Wigner function is not given analytically but has to be computed numerically. Here, the initial sampling is about as time consuming as the propagation, and the run times range between 39 seconds and 64 minutes depending on the number of particles.

5.1. Single Gaussian wave packet. Figure 5.1 illustrates the evolution of kinetic, potential and total energy expectation values for the semiclassical parameters $\varepsilon = 0.1$ and $\varepsilon = 0.001$. The initial sampling uses $N = 10^4$ Halton points, such that the approximate computing time is about 54.6 seconds. As already addressed before in §4.2, the total energy is conserved with an accuracy close to machine precision. The system with $\varepsilon = 0.1$ explores the anharmonicities of the torsional potential in

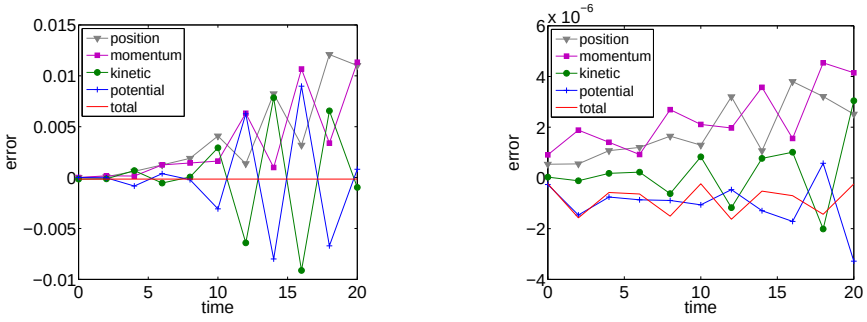

(a) $\varepsilon = 0.1$ (b) $\varepsilon = 0.001$

FIG. 5.2. *Differences between numerically computed expectation values and the references from Strang splitting for the torsional Schrödinger equation with initial Gaussian wave packet (A). The computations use* $N = 10^6$ *Halton points.*

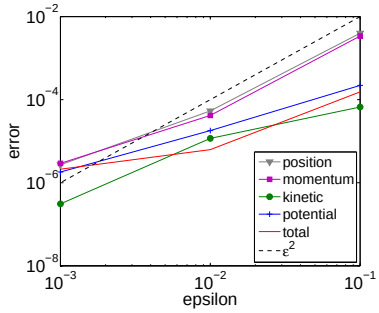

FIG. 5.3. *Differences between numerically computed expectation values and the references from Strang splitting averaged over the time interval* $[0, 20]$ *for different values of* ε*. The dynamics are generated by the torsional Schrödinger equation with initial Gaussian wave packet (A). The results are averaged over ten runs with* $N = 10^6$ *Halton points each. The plot confirms that the method is of second order in* ε*.*

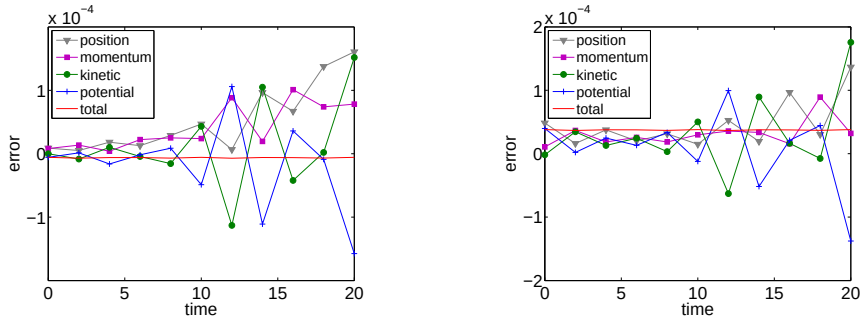

(a) Quasi-Monte Carlo (b) Monte Carlo

FIG. 5.4. *Differences between numerically computed expectation values and references from Strang splitting for the torsional Schrödinger equation with* $\varepsilon = 0.01$ *and two different initial samplings (quasi-Monte Carlo versus Monte Carlo). The results are averaged over ten different runs with* $N = 10^6$ *points each. The initial wave function is the Gaussian wave packet (A).*

a more pronounced way and shows a gradual damping of the kinetic and potential energy oscillations.

We compare the expectation values for position, momentum, kinetic, potential and total energy with reference values from a Strang splitting with Fourier differencing, see appendix §A. For the position and momentum expectation values we consider the norm of the difference. Figure 5.2(a) shows a maximal error increasing by a factor of twelve over time and rising up to 0.013. The drastic ascent after time $t = 10$ is caused by the increasingly anharmonic motion of the the wave function. The snapshots of the dynamics in Figure A.1 of the appendix show a position density losing its elliptical contour around time $t = 8$. Therefore the initial sampling accuracy gets lost and is overridden by the asymptotic accuracy of the approximation. For $\varepsilon = 0.001$, Figure 5.2(b) shows the maximal deviation from the reference value increasing by a factor five and rising up to $5 \cdot 10^{-6}$. For this range of accuracy the comparison of the asymptotic particle method with a grid based reference solution is delicate, since both computations have comparable precision. The L^2-difference of the reference wave function and the one computed on a grid with half the number of grid points per direction is $5.4 \cdot 10^{-6}$, see Table A.1. Therefore Figure 5.2(b) has to be viewed as the comparison of two simulation methods both with an accuracy of the order of 10^{-6}. The oscillatory pattern of the total energy deviation stems from the inaccuracy of the reference solution.

Figure 5.3 shows that the error of the considered expectation values as a function of the semiclassical parameter ε. Each error is averaged over the time interval $[0, 20]$ and ten different sampling realizations with $N = 10^6$ Halton points. As predicted by the Egorov theorem, the results are second order accurate in ε.

Figure 5.4 contrasts the Monte Carlo sampling with the quasi-Monte Carlo approach. In both cases $N = 10^6$ sampling points are used, and the error is the mean error over ten independent runs. The semiclassical parameter is $\varepsilon = 0.01$. For the quasi-Monte Carlo sampling the errors are slightly larger and increase more clearly over time than the ones for the Monte Carlo integration.

5.2. Superposition of Gaussian wave packets. For the superposition of Gaussian wave packets with $\varepsilon = 0.1$, we check whether the cross term can be neglected without loss of accuracy. We validate the particle method against reference values from a converged Strang splitting. It turns out that simulations without cross term ($N = 2 \cdot 10^4$ Halton points) achieve the same accuracy as simulations with the complete Wigner function ($N = 3 \cdot 10^4$ Halton points), see Figure 5.5. The maximal error is below 0.01, while the errors of the position and momentum expectation values even remain smaller. Note, however, that the cross term cannot be neglegted in general because its contribution increases with decreasing distance between the two Gaussians $g_1^\varepsilon(q)$ and $g_2^\varepsilon(q)$.

5.3. Grid based initial data. As a third test case, we simulate the evolution for the torsional potential with $\varepsilon = 0.01$ for an initial datum ϕ_0^ε that stems from the numerical simulation of a molecular laser excitation. The initial position and momentum density have the mean $z_* = (0.4189, 0.0617, -1.0595, 0.0139)$ and the standard deviation $\sigma_* = (0.0639, 0.0759, 0.0834, 0.0780)$, see Figure 5.6(a). We use a uniform density as importance sampling function for the approximation of the initial Wigner function and sample it with the quasi-Monte Carlo method. For this purpose we map N Halton points by the linear transformation

$$[0,1)^4 \to \mathbb{R}^4, \qquad z \mapsto 2\,\mathrm{diag}(\sigma_*)(2z - (1,1,1,1)^T) + z_*.$$

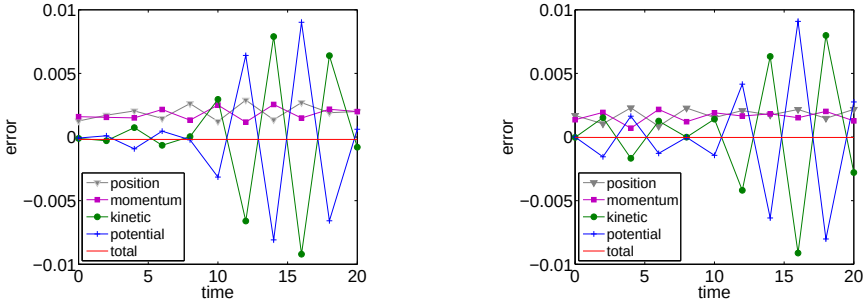

(a) with cross term (b) without cross term

FIG. 5.5. *Accuracy for the simulation with the torsional potential and initial superposition of Gaussian wave packets (B, $\varepsilon = 0.1$). Simulations without cross term achieve the same accuracy as simulations with the complete Wigner function. The results are averaged over ten different runs with $N = 3 \cdot 10^4$ and $N = 2 \cdot 10^4$ Halton points, respectively. The differences between numerically computed observables and reference values from Strang splitting are below 0.01 in both cases.*

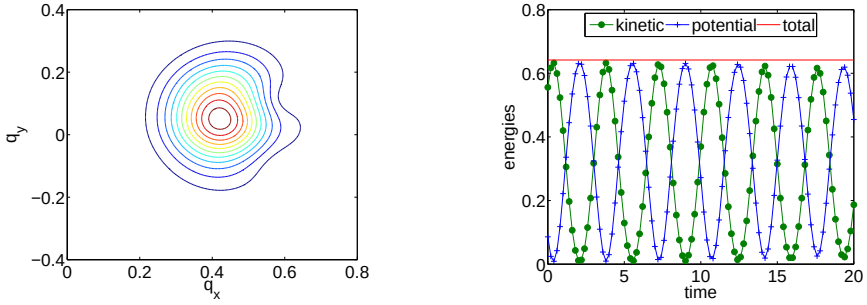

(a) Position density $|\phi_0^\varepsilon(q)|^2$ (b) Evolution of the energies

FIG. 5.6. *Initial position density and evolution of the kinetic, potential, and total energy for the simulation with torsional potential and grid based initial data (C, $\varepsilon = 0.01$). The initial sampling uses $N = 10^3$ Halton points. The computing time is 14.4 seconds.*

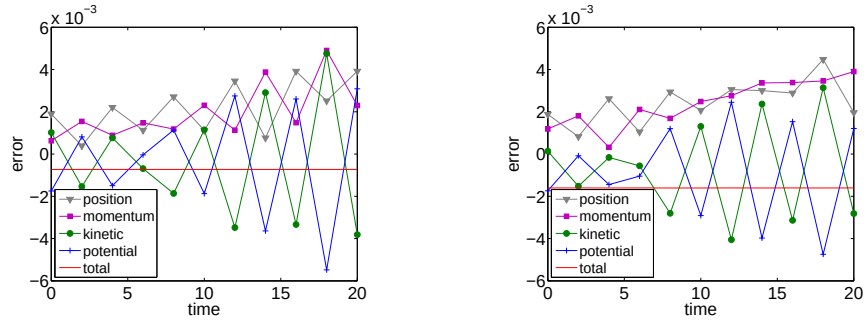

(a) $N = 10^3$ (b) $N = 10^4$

FIG. 5.7. *Differences between numerically computed observables and reference values from Strang splitting for the torsional potential and grid based initial data (C, $\varepsilon = 0.01$). The initial sampling uses $N = 10^3$ and $N = 10^4$ Halton points, respectively. In both cases the maximal error rises from 0.002 at time $t = 0$ to about 0.005.*

The resulting sampling points $\{x_j\}_{j=1}^N$ lie in a rectangle centered around z_* with side length characterized by $4\sigma_*$. Since the Wigner function is a real valued function of integral one, it is split into positive part W_+ and negative part W_- to avoid cancellation. Then we compute expectation values by

$$\langle a \circ \Phi^t \rangle_{\phi_0^\varepsilon} \approx \frac{\sum_{j=1}^{N_+} (a \circ \Phi^t)(x_j) W_+(x_j) + \sum_{j=1}^{N_-} (a \circ \Phi^t)(x_j) W_-(x_j)}{\sum_{j=1}^{N_+} W_+(x_j) + \sum_{j=1}^{N_-} W_-(x_j)}.$$

For the computation of the values of the Wigner function according to

$$W(\phi_0^\varepsilon)(q,p) = (2\pi\varepsilon)^{-2} \int_{\mathbb{R}^2} \mathrm{e}^{\mathrm{i}p\cdot y/\varepsilon} \phi_0^\varepsilon(q - \tfrac{1}{2}y) \overline{\phi}_0^\varepsilon(q + \tfrac{1}{2}y) \mathrm{d}y \tag{5.1}$$

we again use a uniform importance sampling function and quasi-Monte Carlo integration. We generate $n = 500$ Halton points by the two-dimensional mapping $q \mapsto 2\,\mathrm{diag}(\sigma_*(1:2))(2q - (1,1)^T)$. Since the function ϕ_0^ε is only known at the points of the uniform grid specified in Table A.1, each evaluation of the integrand in a quadrature point requires an additional bicubic interpolation with respect to the grid points.

Figure 5.6(b) illustrates the time evolution of the kinetic, potential and total energy. The simulation uses $N = 10^3$ Halton points and takes 14.4 seconds computing time. In Figure 5.7 the errors of the position, momentum, kinetic, potential, and total energy expectation values are shown for an initial sampling with $N = 10^3$ and $N = 10^4$ Halton points in the approximation step. In both cases the maximal initial error of 0.002 rises up to about 0.005. For $N = 10^4$, the position and momentum errors are slightly less oscillatory, but the order of magnitude stays the same as for $N = 10^3$. Contrary to the simulations with analytical initial data, the second order accuracy with respect to the semiclassical parameter is not achieved due to the inexact initial sampling. Neither an increase of the numbers N and n of approximation and quadrature points nor larger rectangles for the domains of integration nor an importance sampling approach improve the situation. The interpolation error for evaluating the Fourier integral (5.1) dominates the initial sampling error.

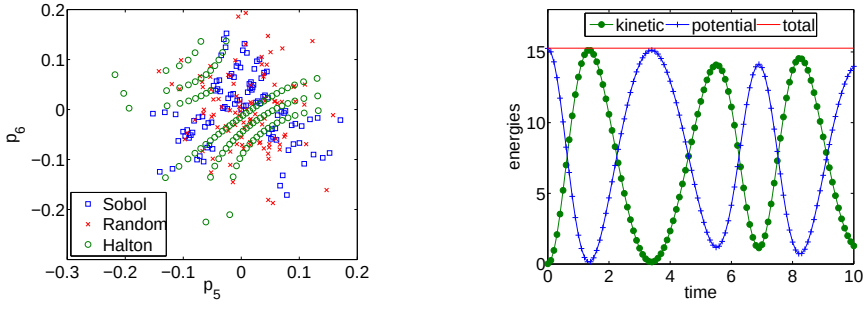

(a) Distribution of sampling points

(b) Evolution of the energies

FIG. 6.1. *Simulations for the six-dimensional Henon-Heiles potential with initial Gaussian wave packet. The eleventh and twelfth coordinates of the Halton sequence align on parallel curves. The evolution of the kinetic, potential, and total energy stems from a simulation with* $N = 100$ *Sobol' points. The approximate computing time is 2.5 seconds.*

6. The Henon-Heiles potential. We conclude with the simulation for the modified six-dimensional Henon-Heiles potential

$$V(q) = \sum_{j=1}^{6} \tfrac{1}{2} q_j^2 + \sum_{j=1}^{5} \sigma_*(q_j q_{j+1}^2 - \tfrac{1}{3} q_j^3) + \tfrac{1}{16}\sigma_*^2 (q_j^2 + q_{j+1}^2)^2$$

with the same choice of the coupling parameter σ_*, the semiclassical parameter ε, and the initial data ψ_0^ε as in [4]. That is, $\sigma_* = 1/\sqrt{80}$, $\varepsilon = 0.01$, and

$$\psi_0^\varepsilon(q) = (\pi\varepsilon)^{-3/2} \exp(-\tfrac{1}{2\varepsilon}|q - q_0|^2), \qquad q_0 = (2,2,2,2,2,2)^T.$$

In this case the phase space has twelve dimensions. For the quasi-Monte Carlo sampling one encounters the well-known tendency of Halton sequences to string together on parallel lines in high dimensions, cf. [14, section 1.1]. Figure 6.1(a) illustrates this effect in plotting coordinates eleven and twelve of three different sampling sets. The first set of sampling points is generated from the Halton sequences associated with the first twelve primes, the second set stems from the twelve dimensional Sobol' sequence, while the third one is randomly chosen from a normal distribution.

$N = 100$ Sobol' points and 2.5 seconds computing time yield the evolution of kinetic, potential and total energy plotted in Figure 6.1(b). Since for a six-dimensional Schrödinger equation a grid based reference solution is no more feasible, we content ourselves with the observation that the numerical results visually resemble those in [4, Figure 5.7]. Moreover, the comparison with analytically computed initial values of kinetic and potential energy in Table 6.1 confirms an accuracy of 10^{-3}.

TABLE 6.1
Accuracy of the initial sampling for the six-dimensional Gaussian wave packet using Halton and Sobol' points. The errors are the absolute deviation from the analytically computed expectation values.

	kinetic energy (Halton/Sobol')	potential energy (Halton/Sobol')
$N = 10^2$	$1.6 \cdot 10^{-4}/1.1 \cdot 10^{-3}$	$7.3 \cdot 10^{-2}/3.9 \cdot 10^{-3}$
$N = 10^3$	$9.1 \cdot 10^{-5}/1.7 \cdot 10^{-4}$	$1.1 \cdot 10^{-2}/5.9 \cdot 10^{-5}$
$N = 10^4$	$2.1 \cdot 10^{-5}/1.9 \cdot 10^{-5}$	$2.2 \cdot 10^{-3}/1.9 \cdot 10^{-4}$

7. Conclusion. The proposed particle method is an efficient tool for computing expectation values for the solution of the nuclear Schrödinger equation in high dimensions. As predicted by the Egorov theorem, the approximation is second order accurate with respect to the semiclassical parameter. The presented numerical experiments solve problems with two- and six-dimensional configuration spaces. They use the same potential functions as [4], and the obtained plots for the time evolution of the kinetic and potential energy expectation values compare nicely. For the initial sampling we have considered a Monte Carlo and quasi-Monte Carlo approach, both achieving comparable accuracy. By construction, all computing times scale linearly in the number of particles and range between three seconds and one hour for $N = 100$ and $N = 3 \cdot 10^5$ points, respectively.

Acknowledgments. We thank M. Weber for suggesting symplectic time integration and P. Deuflhard for advice on improving the first draft of the manuscript.

Appendix A. Reference solutions. For assessing the accuracy of the particle

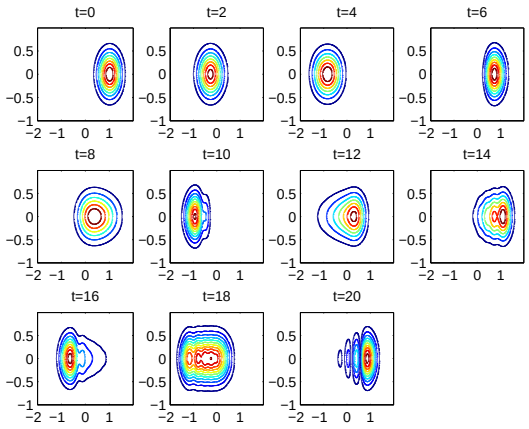

FIG. A.1. *Contour plot of the position density* $q \mapsto |\psi^\varepsilon(q,t)|^2$ *at different times* $t = 0, 2, \ldots, 20$ *for the initial Gaussian wave packet (A,* $\varepsilon = 0.1$*). The Schrödinger equation with torsional potential is solved by the reference solver, a Strang splitting scheme. Around time* $t = 8$ *the wave function loses its elliptical contour.*

method we directly solve the Schrödinger equation with torsional potential (4.2) by a pseudo-spectral Strang splitting scheme. Figure A.1 exemplarily shows contour plots of the position density of the reference solution at different times for the initial Gaussian wave packet (A) with $\varepsilon = 0.1$. For the two-dimensional problem a space discretization based on the fast Fourier transform and a symmetric operator splitting with third order local convergence in time provide accurate reference solutions, see [9]. The time interval $[0, 20]$ is discretized by 5000 time steps for all experiments. All initial wave function are localized on the left and right hand side of the origin and therefore evolve downhill the torsional potential in q_1-direction, see also the snapshots in Figure A.1. Therefore, the computational domains are larger in q_1-direction than in q_2-direction. Table A.1 contains the computational domains, the grid sizes, and the achieved accuracy for different initial data and different values of the semiclassical parameter ε. The accuracy of the solution refers to the difference $\|\psi(t_\mathrm{f}) - \psi_c(t_\mathrm{f})\|_{L^2}$ of the final reference solution $\psi(t_\mathrm{f})$ and a coarser solution $\psi_c(t_\mathrm{f})$, which is computed with four times more grid points. The obtained errors vary between $2.3 \cdot 10^{-4}$ and $5.8 \cdot 10^{-7}$ and are all sufficiently small for the validation of the particle method.

Note, that the generation of such reference solutions is computationally more expensive than the particle method (Table A.2) and as a grid based discretization approach restricted to low-dimensional problems. The solution of the six-dimensional problem considered in §6 is out of reach for this method.

REFERENCES

[1] A. Bouzouina and D. Robert. Uniform semiclassical estimates for the propagation of quantum observables. *Duke Math. J.*, 111:223–252, 2002.

[2] P. Deuflhard and A. Hohmann. *Numerical analysis in modern scientific computing.* Springer-Verlag, 2nd edition, 2003.

[3] M. Dimassi and J Sjöstrand. *Spectral Asymptotics in the Semi-Classical Limit.* Cambridge University Press, Cambridge, 1999.

[4] E. Faou, V. Gradinaru, and C. Lubich. Computing semiclassical quantum dynamics with

TABLE A.1

Input parameters for the reference solution of the Schrödinger equation with torsional potential and accuracy of the wave function at the final time $t_{\mathrm{f}} = 20$.

initial data	ε	domain	fine grid size	accuracy
A	0.1	$[-2,2] \times [-1,1]$	2048×1024	$2.3 \cdot 10^{-4}$
A	0.01	$[-1.4,1.4] \times [-0.35,0.35]$	2048×1024	$1.7 \cdot 10^{-5}$
A	0.001	$[-1.2,1.2] \times [-0.1,0.1]$	2048×1024	$5.4 \cdot 10^{-6}$
B	0.1	$[-2.5,2.5] \times [-1.25,1.25]$	2048×1024	$5.8 \cdot 10^{-7}$
C	0.01	$[-2,2] \times [-1,1]$	1024×512	$6.3 \cdot 10^{-7}$

TABLE A.2

Approximate computing times and memory requirements for the grid based solutions of the Schrödinger equation with torsional potential (4.2) and time interval $[0, 20]$.

grid size	512×256	1024×512	2048×1024
computing time	6 min 42 sec	40 min	2h 47min
memory for ψ_0^ε	2 MB	8 MB	32 MB

Hagedorn wavepackets. *SIAM J. Sci. Comp.*, 31:3027–3041, 2009.

[5] G. Folland. *Harmonic analysis in phase space*. Princeton University Press, 1989.

[6] E. Hairer, C. Lubich, and G. Wanner. *Geometric Numerical Integration*. Springer, 2002.

[7] J. Hartinger, R. Kainhofer, and R. Tichy. Quasi-Monte Carlo algorithms for unbounded, weighted integration problems. *J. Complexity*, 20:654–668, 2004.

[8] W. Hunziker. Distortion analyticity and molecular resonance curves. *Ann. Inst. H. Poincaré Phys. Théor.*, 45(4):339–358, 1986.

[9] T. Jahnke and C. Lubich. Error bounds for exponential operator splitting. *BIT*, 40(4):735–744, 2000.

[10] S. Kube, C. Lasser, and M. Weber. Monte-Carlo sampling of Wigner functions and surface hopping quantum dynamics. *J. Comput. Phys.*, 228(6):1947–1962, 2008.

[11] C. Lubich. *From quantum to classical molecular dynamics: reduced models and numerical analysis*. EMS, Zürich, 2008.

[12] P. A. Markowich, P. Pietra, and C. Pohl. Numerical approximation of quadratic observables of Schrödinger-type equations in the semi-classical limit. *Numer. Math.*, 81:595–630, 1991.

[13] P. Mathé and G. Wei. Quasi-Monte Carlo integration over R^d. *Math. Comp.*, 73(246):827–841, 2004.

[14] W. Morokoff and R. Caflisch. Quasi-Monte Carlo integration. *J. Comput. Phys.*, 122(2):218–230, 1995.

[15] H. Niederreiter. *Random number generation and quasi-Monte Carlo methods*. SIAM, 1992.

[16] H. Spohn and S. Teufel. Adiabatic decoupling and time-dependent Born-Oppenheimer theory. *Comm. Math. Phys.*, 224(1):113–132, 2001.